

# Giant Enhancement of Second Harmonic Generation From WS<sub>2</sub> Monolayer Driven by Nanocavity-Induced Strain

Shimei Liu, Zhenxu Lin, Yuheng Mao, Shulei Li, Mingcheng Panmai, Guixin Li,\* and Sheng Lan\*

Improving the optical nonlinearity of monolayer transition metal dichalcogenides is not only interesting for fundamental research but also highly desirable for practical application. Here, the realization of greatly enhanced second harmonic generation (SHG) is reported in a non-uniformly strained WS<sub>2</sub> monolayer induced by a Si/Au nanocavity. Si/Au nanocavities supporting optical resonances are created at different wavelengths by placing silicon (Si) nanoparticles with different diameters on a thin gold (Au) film, and introduce spatially localized and non-uniform strain in a WS<sub>2</sub> monolayer by transferring the WS<sub>2</sub> monolayer onto such Si/Au nanocavities. A large enhancement is observed in the photoluminescence intensity of the strained WS<sub>2</sub> monolayer. More interestingly, it is found that the SHG from the strained WS<sub>2</sub> monolayer is significantly enhanced by a factor as large as  $\approx 9649$ . This study reveals that the SHG enhancement depends strongly on the magnitude of the strain and exhibits high anisotropy. Moreover, this study demonstrates that the wavelength-dependent SHG enhancement can be manipulated by exploiting the optical resonance supported by the Si/Au nanocavity. These findings suggest the potential applications of non-uniform strain induced by dielectric-metal nanocavities in the development of highly efficient nonlinear optical devices and nanoscaled quantum photonic devices.

properties such as crystal symmetry, polarization domain, and magnetic ordering.<sup>[4–8]</sup> Apart from the well-known phase matching condition for improving SHG efficiency in bulk materials,<sup>[9]</sup> the most commonly used methods for enhancing SHG in 2D transition-metal dichalcogenides (TMDCs) include engineering the inversion symmetry of crystals and enhancing light-matter interaction.<sup>[10]</sup> While the former method focuses on the choice of appropriate second-order nonlinear susceptibility ( $\chi_o^{(2)}$ ) of the crystalline materials, the latter one mainly involves the resonance enhancement of the electric field of light at the fundamental and/or second harmonic wavelengths. So far, various strategies have been proposed to manipulate the crystal structure of 2D materials, including the use of twisted layers,<sup>[11]</sup> strain,<sup>[12]</sup> defect,<sup>[13,14]</sup> and external electric or magnetic fields.<sup>[15,16]</sup> Among them, strain engineering emerges as a simple and powerful way to modify the electrical and optical properties of

materials. For example, it has been exploited to change the bandgap<sup>[17–21]</sup> and realize single photon emission.<sup>[22]</sup>

TMDCs represent an ideal platform for strain engineering due to their high flexibility and mechanical strength.<sup>[23]</sup> It has been demonstrated that uniform strain can be imposed

## 1. Introduction

Second harmonic generation (SHG) is one of the most important nonlinear optical processes that has been widely employed for frequency conversion in various spectral regimes.<sup>[1–3]</sup> This technique also has important applications in identifying material

S. Liu, Y. Mao, S. Lan  
Guangdong Provincial Key Laboratory of Nanophotonic Functional Materials and Devices  
School of Optoelectronic Science and Engineering  
South China Normal University  
Guangzhou 510006, P. R. China  
E-mail: slan@scnu.edu.cn  
Z. Lin  
School of Material Science and Engineering  
Hanshan Normal University  
Chaozhou 521041, P. R. China

S. Li  
School of Optoelectronic Engineering  
Guangdong Polytechnic Normal University  
Guangzhou 510665, P. R. China  
M. Panmai  
Division of Physics and Applied Physics  
School of Physical and Mathematical Sciences  
Nanyang Technological University  
Singapore 637371, Singapore  
G. Li  
Department of Materials Science and Engineering & Institute for Applied Optics and Precision Engineering  
Southern University of Science and Technology  
Shenzhen 518055, P. R. China  
E-mail: ligx@sustech.edu.cn

The ORCID identification number(s) for the author(s) of this article can be found under <https://doi.org/10.1002/lpor.202500468>

DOI: 10.1002/lpor.202500468

on TMDC monolayers via stretching or bending, leading to modification of bandgaps and photoluminescence (PL) properties.<sup>[20,24,25]</sup> On the other hand, non-uniform strain can be induced in the wrinkles and nano-bubbles formed in a TMDC monolayer<sup>[21,26–30]</sup> or by transferring a TMDC monolayer on periodic nanostructures<sup>[31–33]</sup> or individual nanoparticles.<sup>[34,35]</sup> In these cases, the non-uniform strain creates local potential wells in the conduction and valence bands which result in the increase of local carrier density.<sup>[31,33,36]</sup> The recombination of the excitons confined in the potential wells is accelerated, leading to the enhancement of PL intensity. This kind of phenomenon was experimentally observed in the MoS<sub>2</sub> monolayer draped on periodic nanostructures,<sup>[31,33]</sup> wrinkled WS<sub>2</sub> monolayer,<sup>[21,37]</sup> monolayer WS<sub>2</sub> nanobubble,<sup>[38]</sup> and a WS<sub>2</sub> monolayer indented by the tip of an atomic force microscope (AFM).<sup>[36]</sup>

It is expected that strain engineering can be used to effectively modify the second-order nonlinear optical property of a TMDC monolayer.<sup>[10,39]</sup> In previous works, it is reported that uniform uniaxial strain may lead to reduced SHG intensity.<sup>[40–42]</sup> In comparison, the wrinkle-type non-uniform strain in TMDCs may lead to a SHG enhancement.<sup>[43]</sup> Moreover, a 35-fold enhancement in SHG efficiency was found in the wrinkles of a NbOI<sub>2</sub> flake when the strain is applied along its polar direction.<sup>[12]</sup> Due to pseudo-Landau levels induced by non-uniform strain,<sup>[44]</sup> SHG intensity from a graphene monolayer is enhanced by a factor of  $\approx 50$  at low temperatures due to sublattice polarization.<sup>[45]</sup> More interestingly, the wrinkle nanostructures in CuInP<sub>2</sub>S<sub>6</sub> flake exhibit a 160-fold enhancement of SHG.<sup>[46]</sup> Recently, it was found that the SHG in the multilayer NbOI<sub>2</sub> can be enhanced by a factor of  $\approx 3$  by applying a pressure of 2.5 GPa to tune the displacement of Nb atoms.<sup>[47]</sup> All these phenomena indicate that the SHG of a TMDC monolayer can be modified by using spatially localized strain.

A spatially localized strain is generally non-uniform and it can be induced in a TMDC monolayer by using a metallic nanoparticle. However, the electric field enhancement on the surface of the metallic nanoparticle originating from the surface plasmon resonance may also lead to the SHG enhancement. In this case, it is difficult to evaluate the effect of strain on the SHG. A particle-on-film system, which is composed of a metallic (or dielectric) nanoparticle placed on a thin metal film, also supports a localized plasmon mode with greatly enhanced electric field in the gap between the nanoparticle and the film. However, the localized plasmon mode supported by such a system has little effect on the TMDC monolayer placed on the top of the nanoparticle. So far, many efforts have been devoted to the enhancement of light-matter interaction between TMDC monolayers and nanocavities, whose properties can be modified by changing the optical environments at the subwavelength scale.<sup>[48–50]</sup> For example, it was reported that the SHG of a TMDC monolayer can be enhanced by two to three orders of magnitude by exploiting the enhanced electric field in the plasmonic nanostructures.<sup>[51]</sup> Therefore, it is expected that the SHG of a TMDC monolayer can be modified not only by the non-uniform strain induced by the nanoparticle but also the optical resonances supported by the particle-on-film system.

In this work, we propose to enhance the SHG efficiency of a WS<sub>2</sub> monolayer by exploiting the spatially localized strain induced by a nanocavity composed of a silicon (Si) nanoparticle and a thin gold (Au) film. We observed significantly enhanced SHG

from the WS<sub>2</sub> monolayer arising from both the strain-modified nonlinear susceptibility and the cavity enhancement effect. Compared with the WS<sub>2</sub>/Au planar structure, the SHG intensity from the nanocavity is enhanced by a factor of  $\approx 9649$ .

## 2. Results and Discussion

### 2.1. Spatially Localized Strain in the WS<sub>2</sub> Monolayer Induced by a Silicon Nanoparticle

**Figure 1a** shows the schematic of the WS<sub>2</sub>/Si/Au nanocavity, which is fabricated on a glass (SiO<sub>2</sub>) substrate. The nanocavity is composed of a WS<sub>2</sub> monolayer, a silicon nanoparticle, and a thin gold film. The WS<sub>2</sub> monolayer is grown by chemical vapor deposition (CVD) method and transferred onto the Si/Au nanocavity with the wet-transfer method (see Methods for details). It is expected that the SHG from the WS<sub>2</sub> monolayer will be dramatically affected by the spatially localized strain. From the scanning electron microscopy (SEM) image of a typical WS<sub>2</sub>/Si/Au nanocavity (**Figure 1b**), one can identify the WS<sub>2</sub> monolayer draped on the silicon nanoparticle. As shown in **Figure 1c**, the morphology of the WS<sub>2</sub>/Si/Au nanocavity is also characterized by using AFM (also see Note S1, Supporting Information). From the height profile of the deformed WS<sub>2</sub> monolayer (**Figure 1d**), it can be seen clearly that the contacting area between the WS<sub>2</sub> monolayer and the silicon nanoparticle is spatially localized. From the dark-field microscope image, we can identify the position of each individual WS<sub>2</sub>/Si/Au nanocavity, as shown by the dashed circle in **Figure 1e**. In **Figure 1f**, we present the PL mapping of the sample obtained by using 532 nm continuous wave (CW) laser light (also see **Figure S2**, Supporting Information). One can clearly identify the enhanced PL intensity from the WS<sub>2</sub>/Si/Au nanocavity. Moreover, the SHG mapping of the nanocavity and surrounding area was carried out by using 800 nm femtosecond (fs) laser light, as shown in **Figure 1g**. Similarly, one can see the SHG enhancement at the nanocavity. Based on numerical simulation, the electric field enhancement on the top of the silicon nanoparticle is weak (see Note S3, Supporting Information), indicating that the enhanced SHG does not arise from the electric field enhance-

### 2.2. Greatly Enhanced PL From the WS<sub>2</sub>/Si/Au Nanocavity

In **Figure 2a**, we present the forward and backward scattering spectra of five WS<sub>2</sub>/Si/Au nanocavities. The optical images of the forward scattered light recorded by using a charge coupled device (CCD) are shown in the insets. In each case, a characteristic peak is observed in the forward scattering spectrum, which is attributed to the mirror-image-induced magnetic dipole (MMD) resonance supported by the WS<sub>2</sub>/Si/Au nanocavity.<sup>[52]</sup> Based on the scattering light color which is changed from green to orange and finally to red, the diameter ( $D$ ) of the silicon nanoparticle is estimated to be in the range of 150–210 nm. In **Figure 2b**, we show the PL spectra measured for the five WS<sub>2</sub>/Si/Au nanocavities (see also Note S4, Supporting Information). In each case, the PL spectrum measured for the adjacent WS<sub>2</sub>/Au planar structure is provided for reference. It is noticed that the PL intensity

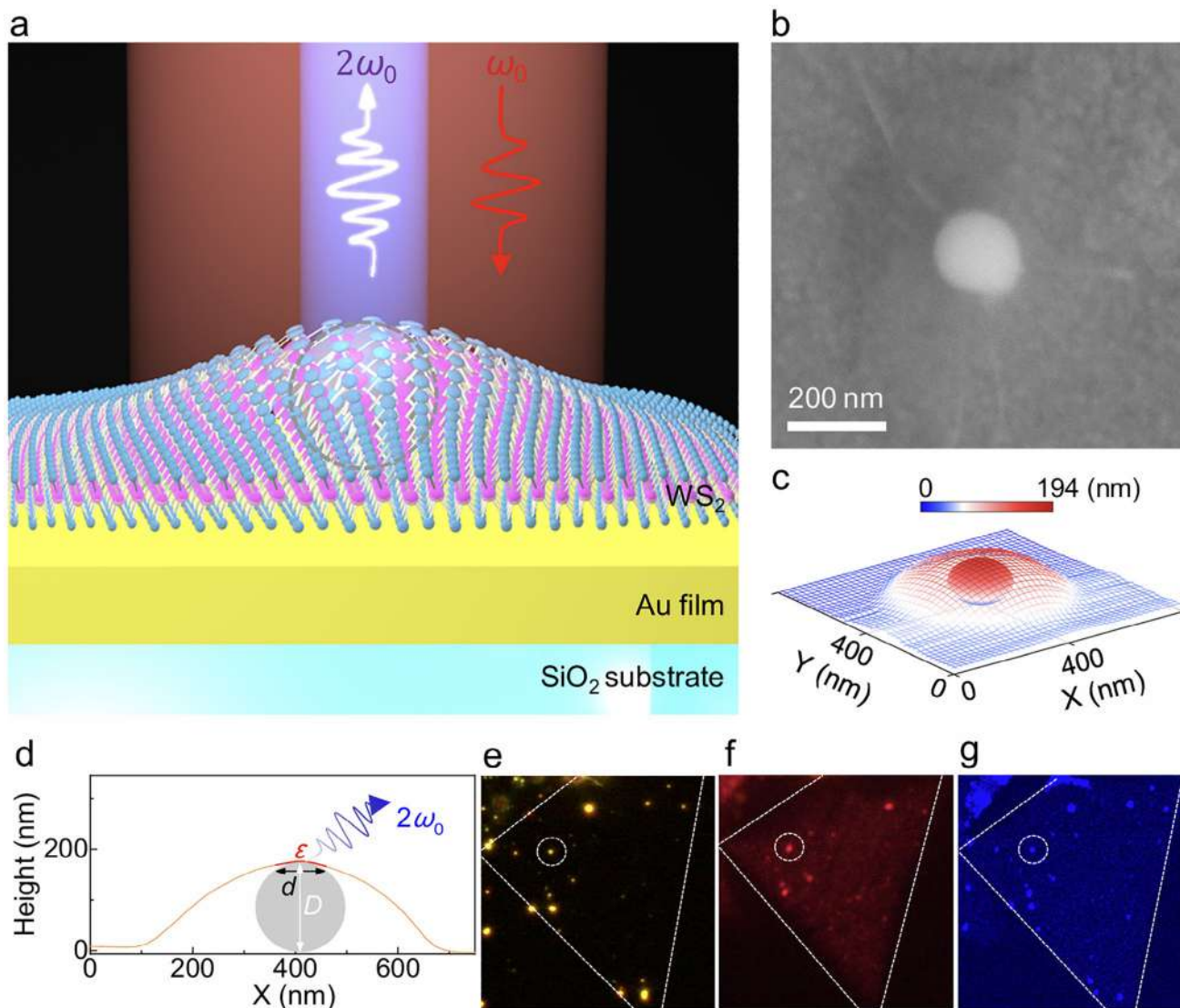


**Figure 1.** Nonuniform strain in a  $\text{WS}_2$  monolayer induced by a Si/Au nanocavity. a) Schematic diagram of a silicon nanoparticle draped with a  $\text{WS}_2$  monolayer, which enables the enhanced SHG (purple light) near the top of the silicon nanoparticle upon the excitation of a fs laser (red light). b) SEM image of a strained  $\text{WS}_2$  monolayer on a silicon nanoparticle. c) The typical AFM topography of a strained  $\text{WS}_2$  monolayer. The small sphere covered inside represents the silicon nanoparticle. d) Height profile extracted from the AFM image in c). The dark-field microscope image, PL mapping image, and SHG mapping image of the  $\text{WS}_2/\text{Si}/\text{Au}$  nanocavity (enclosed by the dashed circle) are shown in (e–g), respectively.

of the unstrained Si/ $\text{WS}_2$ /Au nanocavity is reduced due to the strong coupling between the exciton and MMD resonance (see Note S5, Supporting Information).<sup>[53]</sup> In contrast, it is observed that the PL intensities of the five strained  $\text{WS}_2/\text{Si}/\text{Au}$  nanocavities are greatly enhanced due to the exciton funneling effect. For clarity, we use a relative intensity defined as  $(I - I_0)/I_0$  to evaluate the enhanced PL intensity of a  $\text{WS}_2/\text{Si}/\text{Au}$  nanocavity ( $I$ ) with respect to that of the  $\text{WS}_2/\text{Au}$  planar structure ( $I_0$ ). It is noticed that a relative intensity  $((I - I_0)/I_0)$  as large as  $\approx 11$  is observed in nanocavity D. This value is much larger than those reported for strained 2D materials,<sup>[31,36,37]</sup> such as non-uniformly strained  $\text{MoS}_2$  monolayer induced by Au nanostructure and  $\text{WS}_2$  wrinkle structure.<sup>[21,33]</sup> Although the redshift of PL peak and the enhancement of PL intensity induced by spatially localized strain are clearly identified in all  $\text{WS}_2/\text{Si}/\text{Au}$  nanocavities (see Figure 2b),

the shift of Raman peak, which is commonly used to characterize the extent of strain, was not observed in the Raman spectrum (see Figure S1c, Supporting Information). It is ascribed to the limited spatial resolution of the Raman spectroscopy owing to a large laser spot size compared to the strained area in a  $\text{WS}_2/\text{Si}/\text{Au}$  nanocavity. Owing to the exciton funnel effect and quantum confinement effect, the strained area exhibits a significantly enhanced PL intensity. This is the reason why the redshift of the PL peak can be revealed in the PL spectrum. In comparison, the strain-induced shift of the Raman peak is not observed in the Raman spectrum because the Raman scattering intensity is not enhanced by the strain. Thus, we can conclude that the size of the strained area is much smaller than that of the laser spot. Based on the AFM image shown in Figure 1d, we assumed that the diameter ( $d$ ) of strained region is close to  $\approx 100$  nm, which

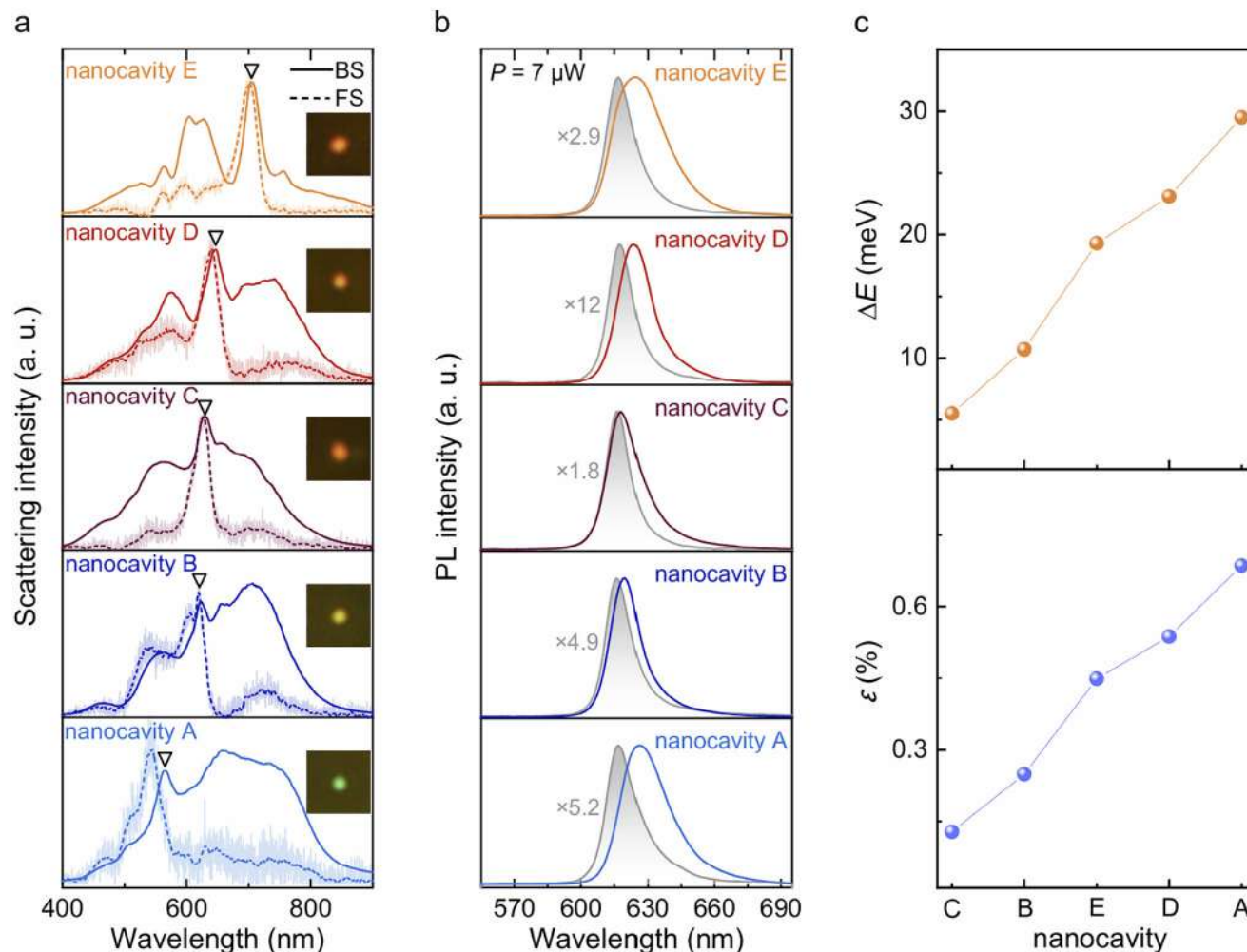


**Figure 2.** Greatly enhanced PL intensity from the  $\text{WS}_2/\text{Si}/\text{Au}$  nanocavities. a) Forward and backward scattering (FS and BS) spectra measured for the five  $\text{WS}_2/\text{Si}/\text{Au}$  nanocavities (nanocavity A-E) composed of silicon nanoparticles with different diameters. The CCD images of the corresponding forward scattering light are shown in the insets. b) PL spectra measured for the five strained  $\text{WS}_2/\text{Si}/\text{Au}$  nanocavities by using 488 nm laser light at  $P = 7 \mu\text{W}$  (colored curves). The PL spectra of the  $\text{WS}_2/\text{Au}$  planar structures (shaded areas) are also provided for comparison. c) Reduced bandgap energies ( $\Delta E$ ) (upper panel) and strain values ( $\epsilon$ ) (lower panel) extracted for the five  $\text{WS}_2/\text{Si}/\text{Au}$  nanocavities from the shift of the PL peak.

is approximately half of the diameter of the silicon nanoparticle. In addition, the radius of the strained region ( $\approx 50 \text{ nm}$ ) is smaller than the diffusion length of photogenerated excitons in  $\text{WS}_2$  monolayer ( $\approx 180 \text{ nm}$ ).<sup>[36]</sup> Furthermore, it is expected that the drift of excitons induced by strain is dominant over diffusion ( $< 250 \text{ nm}$ ).<sup>[36,37]</sup> Since the area of the strained region in a  $\text{WS}_2/\text{Si}/\text{Au}$  nanocavity is much smaller than that of the laser spot, it is expected that the actual enhancement factor ( $EF$ ) of the PL intensity will be much greater than that observed in the experiment. Basically, one can derive the  $EF$  of PL intensity in the strained region by using the following formula:

$$EF = \frac{\int_{S_0} I(x, y) dS}{\int_{S_2} I(x, y) dS} \cdot \frac{I - I_0}{I_0} \quad (1)$$

where  $I(x, y)$  is the intensity distribution of the laser beam,  $S_0$  is the area at the full width at half maximum of  $I(x, y)$ , and  $S_2$  is the area of the strained  $\text{WS}_2$ . For the  $\text{WS}_2/\text{Si}/\text{Au}$  nanocavities

investigated in this work, the largest  $EF$  in the PL intensity is found to be  $\approx 1144$  in nanocavity D.

In Figure 2b, one can see the redshift of the PL peak and the linewidth broadening, which are caused by the reduced bandgap and increased contribution of trions induced by the strain.<sup>[36]</sup> By fitting the PL spectra with multiple Lorentz lineshapes, one can extract the resonant wavelengths and linewidths of excitons and trions. In Figure 2c, we present the bandgap energy changes observed for the five nanocavities. Apparently, the largest change ( $\approx 29.5 \text{ meV}$ ) in the bandgap energy is observed in nanocavity A. Based on the modulation rate ( $\approx 43 \text{ meV}/\%$ ) of the bandgap energy reported for  $\text{WS}_2$  monolayer,<sup>[24]</sup> the average strain ( $\epsilon$ ) imposed on the  $\text{WS}_2$  monolayer is estimated to be  $\approx 0.69\%$ . It should be emphasized, however, the strain induced by the silicon nanoparticle is non-uniform and spatially localized because of the non-spherical shape and non-smooth surface. For nanocavity A, the changes in the resonant energies of excitons and trions are derived to be  $\approx 26.5$  and  $\approx 43.1 \text{ meV}$ , respectively (see Figure S6b, Supporting Information). Since the blueshift of the

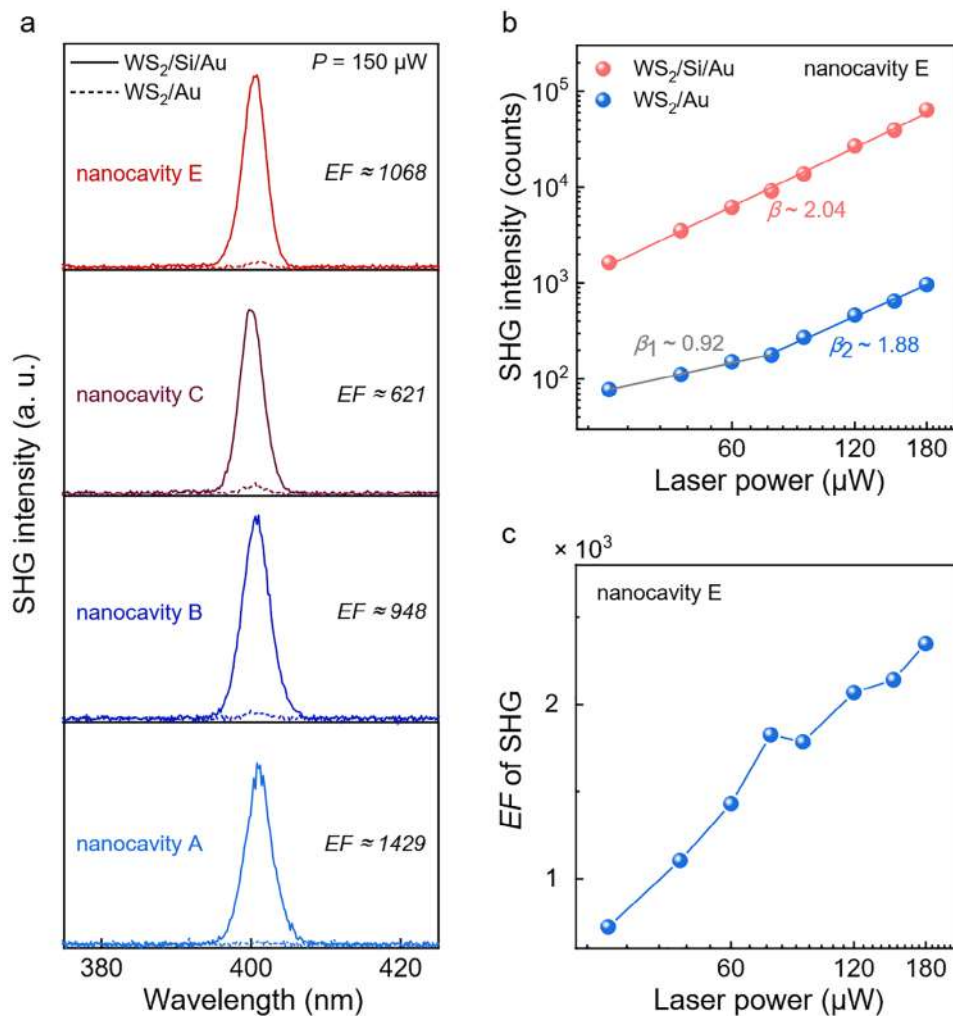


**Figure 3.** Greatly enhanced SHG intensity from the WS<sub>2</sub>/Si/Au nanocavities. a) SHG spectra measured for four strained WS<sub>2</sub>/Si/Au nanocavities (nanocavity A, B, C, and E) (solid curves) at  $P = 150 \mu\text{W}$ . The SHG spectra of the WS<sub>2</sub>/Au planar structures (dashed curves) are provided for comparison. In each case, the SHG  $EF$  of the WS<sub>2</sub>/Si/Au nanocavity is provided, and the excitation wavelength is fixed at 800 nm. b) Log plot of the laser power dependence of integrated SHG intensity observed for the WS<sub>2</sub>/Si/Au nanocavity (nanocavity E) and the WS<sub>2</sub>/Au planar structure. The slope ( $\beta$ ) of the plot is  $\approx 2.0$ . c) Dependence of the SHG  $EF$  on the pumping power observed for the WS<sub>2</sub>/Si/Au nanocavity (nanocavity E).

PL peak and narrowing of PL linewidth are usually observed in a suspended WS<sub>2</sub> monolayer,<sup>[54,55]</sup> we can conclude that the enhanced PL intensities observed in WS<sub>2</sub>/Si/Au nanocavities are mainly caused by the strain. If we inspect the ratio of the intensity of trions to that of excitons ( $I_t/I_e$ ), it is found that in most cases the WS<sub>2</sub>/Si/Au nanocavity exhibits a larger value than that of the WS<sub>2</sub>/Au planar structure (see Figure S7a, Supporting Information). This feature indicates the efficient conversion of excitons to trions due to the non-uniform strain induced by a silicon nanoparticle. Similar phenomena were also demonstrated by using AFM tip and plasmonic waveguide.<sup>[36,56]</sup>

### 2.3. Enhanced SHG from the WS<sub>2</sub>/Si/Au Nanocavity

In order to verify the effect of spatially localized strain on the SHG from the WS<sub>2</sub> monolayer, we performed SHG measurements on four WS<sub>2</sub>/Si/Au nanocavities (A, B, C, E) by using the fs laser at

the wavelength of 800 nm. As shown in Figure 3a (also see Figure S4c, Supporting Information), the SHG from the four nanocavities and the adjacent planar areas are characterized. Basically, one can derive the  $EF$  of SHG intensity in the strained region by using the following formula:

$$EF = \frac{\int_{S_1} I^2(x, y) dS}{\int_{S_2} I^2(x, y) dS} \cdot \frac{I - I_0}{I_0} \quad (2)$$

where  $S_1$  is the area at the full width at half maximum of  $I^2(x, y)$ . It is found that the  $EF$ s of SHG intensity in these WS<sub>2</sub>/Si/Au nanocavities are about three orders of magnitude, confirming the repeatability of the nanocavity fabrication. Interestingly, it is noticed that the  $EF$  is strongly correlated with the magnitude of strain (see Figure S6a, Supporting Information). The greatly enhanced SHG intensity observed in the WS<sub>2</sub>/Si/Au nanocavity arises mainly from the strain rather than the enhanced electric

field (see Note S8, Supporting Information). For nanocavity A, the maximum relative intensity was found to be  $\approx 40.8$  at a laser power of  $P = 150 \mu\text{W}$ . Therefore, an  $EF$  is derived as large as  $\approx 1429$ . In addition, we used the  $\text{WS}_2$  monolayer placed on the Au film (i.e., the  $\text{WS}_2/\text{Au}$  planar structure) as the reference sample. In this way, the influence of defects or impurities on the SHG intensity will be cancelled out in the evaluation of the  $EF$  induced by strain. One might think that the giant enhancement of the SHG is partially due to the quenching effect introduced by the metallic contact. However, it was revealed that the effect of substrate on the SHG intensity is much smaller than that of the strain (see Note S9, Supporting Information). To verify this, we also measured the SHG intensity of the suspended  $\text{WS}_2$  monolayer. Indeed, the SHG intensity of a suspended  $\text{WS}_2$  monolayer is  $\approx 12.9$  times stronger than that of the  $\text{WS}_2/\text{Au}$  planar structure (see Note S9, Supporting Information). This indirectly indicates that the giant enhancement of SHG mainly comes from the spatially localized strain induced by the silicon nanoparticle. In order to further understand the nonlinear optical properties of the  $\text{WS}_2/\text{Si}/\text{Au}$  nanocavities, we performed SHG measurements at different pumping powers. In Figure 3b, it can be seen that the power dependence of the SHG intensity in nanocavity E exhibits a slope value of  $\approx 2.04$  (see also Note S10, Supporting Information), confirming the second order nonlinear optical process. In comparison, it is noticed that the slope value of the SHG signals from the  $\text{WS}_2/\text{Au}$  planar structure is smaller than 2.0 at low pumping powers, indicating the weak nonlinear optical response. In Figure 3c, the  $EF$ s derived for nanocavity E at different pumping powers are summarized. It indicates that the  $EF$  of a  $\text{WS}_2/\text{Si}/\text{Au}$  nanocavity strongly depends on the pumping power. As the pumping power increases, the  $EF$  becomes larger and reaches  $\approx 2347$  when the pumping power is  $\approx 180 \mu\text{W}$  (also see Note S10, Supporting Information). This behavior implies that the thermal expansion of the crystal lattice in the strained region of the  $\text{WS}_2$  monolayer can be induced by the laser irradiation, which further increases the nonlinear optical susceptibility.

#### 2.4. Wavelength-Dependent SHG Intensity of the $\text{WS}_2/\text{Si}/\text{Au}$ Nanocavities

In general, the SHG intensity of a TMDC monolayer is wavelength dependent. In the previous study, it was found that the wavelength-dependent SHG intensity of  $\text{WS}_2$  monolayer can be modified by strain.<sup>[57]</sup> In this work, we carried out SHG measurements for the  $\text{WS}_2/\text{Au}$  planar structure by using excitation wavelengths  $\lambda_{\text{ex}}$  ranging from 740 to 850 nm, as shown in Figure 4a. It is noticed that the SHG intensity first increases and then decreases with the increasing excitation wavelength. The maximum SHG intensity is observed at  $\lambda_{\text{ex}} = 810$  nm. In order to exclude the influence of the enhanced electric field induced by the optical mode on the SHG intensity, we selected a non-silicon nanoparticle (P1) without obvious optical resonance in the scattering spectrum and performed the SHG measurements for the  $\text{WS}_2/\text{P1}/\text{Au}$  nanocavity (see Figure S14a,b, Supporting Information). In Figure S14b (Supporting Information), it can be seen that the SHG intensity of  $\text{WS}_2/\text{P1}/\text{Au}$  nanocavity increases rapidly when the excitation wavelength is increased from 740 to 840 nm. Then, a slight decrease in the SHG intensity is observed

as the excitation wavelength is further increased to 850 nm. Apparently, the dependence of the SHG intensity on the excitation wavelength observed in  $\text{WS}_2/\text{P1}/\text{Au}$  nanocavity is different from that observed in the  $\text{WS}_2/\text{Au}$  planar structure. This behavior is attributed to the modification of  $\chi_o^{(2)}$  induced by the strain. In fact, it was reported that tensile strain in biaxial direction will lead to an increase in the  $\chi_o^{(2)}$  of  $\text{WS}_2$  monolayer for photon energy ranging from 0.5 to 1.5 eV.<sup>[57]</sup> In addition, the wavelength at which the maximum SHG intensity is achieved is redshifted with increasing strain. This feature is responsible for the SHG enhancement observed for  $\text{WS}_2/\text{P1}/\text{Au}$  nanocavity at longer excitation wavelength. Apart from strain, the SHG intensity of a  $\text{WS}_2/\text{Si}/\text{Au}$  nanocavity is also affected by the electric field enhancement induced by the MMD resonance supported by the nanocavity. In Figure 4b,c, we present the backward scattering spectra measured (red solid curves) and calculated (blue solid curves) for two  $\text{WS}_2/\text{Si}/\text{Au}$  nanocavities. Physically, the SHG intensity of a  $\text{WS}_2/\text{Si}/\text{Au}$  nanocavity at an excitation wavelength can be evaluated by the integration of  $|E|^4$  over the volume of the strained region (i.e.,  $I_{\text{SHG}} \propto [\int |E(\lambda_{\text{ex}})|^4 dV]/V$ ). In Figure 4d, we show the spectra of  $I_{\text{SHG}}(\lambda_{\text{ex}})$  calculated for the two  $\text{WS}_2/\text{Si}/\text{Au}$  nanocavities (see also Note S12, Supporting Information). It is noticed that the two nanocavities exhibit completely different behaviors. With increasing excitation wavelength, the SHG intensity of nanocavity F ( $D = 190$  nm) increases rapidly and becomes saturated. In comparison, the SHG intensity of nanocavity E ( $D = 210$  nm) decreases rapidly and then increases gradually after reaching a minimum value at 790 nm. For a  $\text{WS}_2/\text{Si}/\text{Au}$  nanocavity, the electric field enhancements at shorter wavelengths mainly originate from the MMD resonance ( $\approx 705$  nm) while those at longer wavelengths arise from other optical resonances, such as the interference between the magnetic dipole excited in the silicon nanoparticle and its mirror image induced by the gold film. In Figure 4e,f, we present the SHG spectra measured at different excitation wavelengths for the two nanocavities. At first glance, the dependence of the SHG intensity on the excitation wavelength observed in nanocavity F is quite similar to that observed in the  $\text{WS}_2/\text{P1}/\text{Au}$  nanocavity. However, it is noticed that the relative SHG intensity of nanocavity F at the longer wavelengths with respect to that at the shorter wavelengths is larger than that observed in  $\text{WS}_2/\text{P1}/\text{Au}$  nanocavity. This behavior is caused by the enhanced electric field of the optical resonance supported by nanocavity F. For nanocavity E, it is found that the SHG intensity is enhanced at excitation wavelengths of 740–760 nm, as shown in Figure 4f. It originates from the electric field enhancement induced by the MMD excited in nanocavity E. In addition, a rapid decrease in the SHG intensity is observed when the excitation wavelength is increased from 820 to 850 nm. It has been known that the wavelength-dependent nonlinear optical response of a  $\text{WS}_2$  monolayer will be modified by the uniform biaxial strain exerted on the  $\text{WS}_2$  monolayer. The non-uniform and spatially localized strain generated by a Si/Au nanocavity may further alter the wavelength-dependent nonlinear optical response of the  $\text{WS}_2$  monolayer. Combined with the optical resonance supported by the nanocavity, the nanocavities investigated in this work exhibit different wavelength-dependent nonlinear optical behaviors. In this work, the largest  $EF$  of SHG induced by a  $\text{WS}_2/\text{Si}/\text{Au}$  nanocavity is found to be  $\approx 9649$  (see Figure S14d,f, Supporting

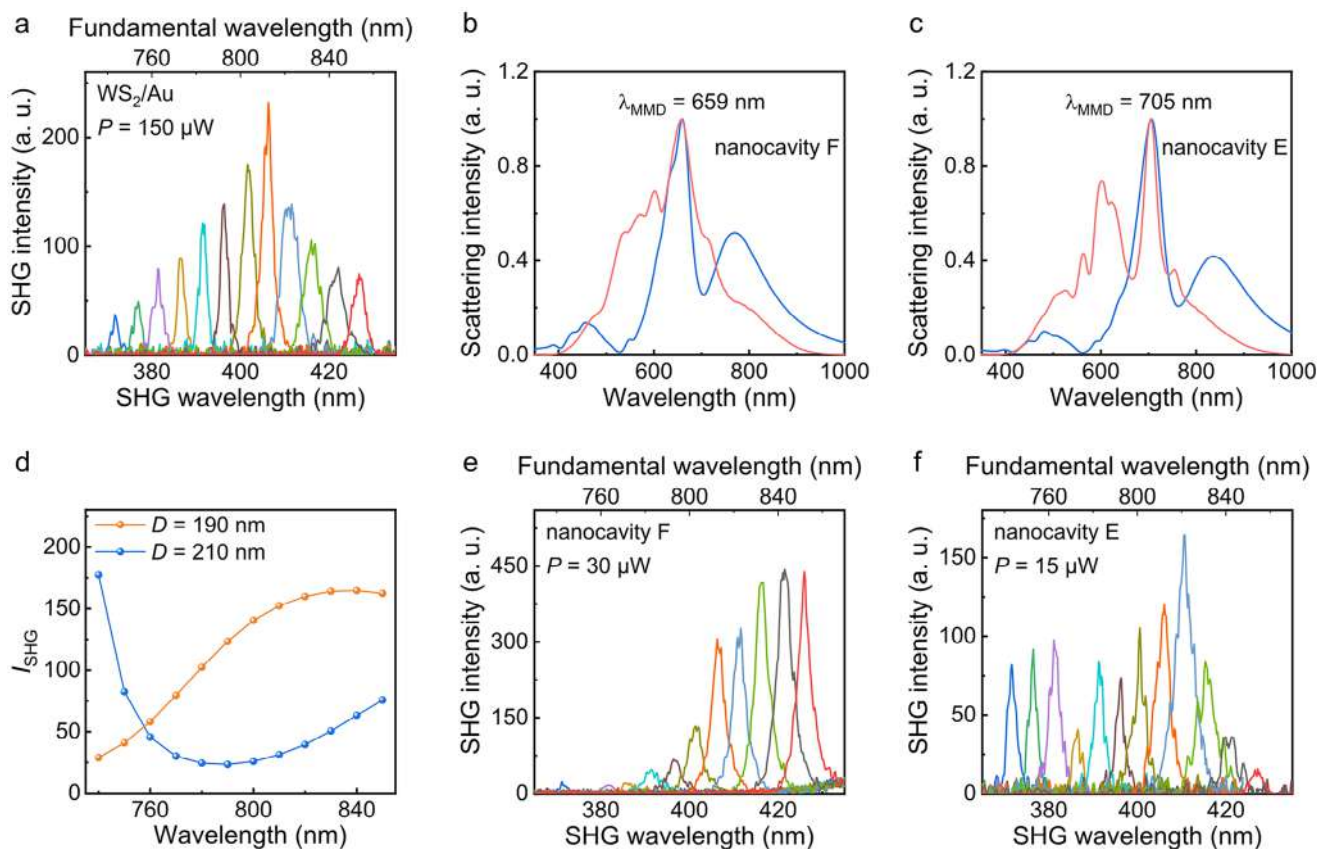


**Figure 4.** Wavelength-dependent SHG intensity of a  $\text{WS}_2/\text{Si}/\text{Au}$  nanocavity. a) The wavelength-dependent SHG intensity measured for the  $\text{WS}_2/\text{Au}$  planar structure at pumping power of  $P = 150 \mu\text{W}$ . b, c) Backward scattering spectra (red solid curves) measured for two  $\text{WS}_2/\text{Si}/\text{Au}$  nanocavities (nanocavity F and E). The backward scattering spectra (blue solid curves) calculated for the two  $\text{WS}_2/\text{Si}/\text{Au}$  nanocavities with a diameter  $D = 190 \text{ nm}$  b) and  $D = 210 \text{ nm}$  c) are provided for comparison. d) Wavelength-dependent SHG intensity calculated for the two  $\text{WS}_2/\text{Si}/\text{Au}$  nanocavities with diameter  $D = 190 \text{ nm}$  and  $D = 210 \text{ nm}$ , respectively. e, f) The wavelength-dependent SHG intensity measured for the two  $\text{WS}_2/\text{Si}/\text{Au}$  nanocavities (nanocavity F and E).

Information). This behavior indicates that the SHG intensity of a strained  $\text{WS}_2/\text{Si}/\text{Au}$  nanocavity depends strongly on the excitation wavelength.

### 2.5. Polarization-Dependent SHG Intensity of the $\text{WS}_2/\text{Si}/\text{Au}$ Nanocavity

Apart from excitation wavelength, it has been known that the SHG intensity of a  $\text{WS}_2$  monolayer strongly depends on the polarization of the excitation light. Under the excitation of a linearly polarized light, the polarization-dependent SHG intensity exhibits a 6-fold symmetry which is consistent with its crystal structure. Since the crystal structure of the  $\text{WS}_2$  monolayer can be modified by the non-uniform strain, it is expected that the polarization-dependent SHG intensity can be greatly changed in a strained  $\text{WS}_2/\text{Si}/\text{Au}$  nanocavity. From another point of view, it implies that the magnitude of strain can be characterized by the polarization-dependent SHG intensity.<sup>[42]</sup> Since the nonlinear optical responses of the  $\text{WS}_2$  monolayer is strong at the excitation wavelength of  $800 \text{ nm}$  and the  $\text{WS}_2$  monolayer possesses a low thermal conductivity, a reduction in the SHG intensity

is usually observed during the polarization-dependent measurement due to heat accumulation, which will affect its potential applications. This behavior may affect the accuracy of the experimental results. Also, considering that the SHG of  $\text{WS}_2$  monolayer is more sensitive to strain at longer excitation wavelength, we carried out polarization-dependent SHG intensity measurement for a strained  $\text{WS}_2/\text{Si}/\text{Au}$  nanocavity (nanocavity G) by using a linearly polarized light at  $\lambda_{\text{ex}} = 1064 \text{ nm}$ , as shown in **Figure 5a** (see also Note S13, Supporting Information). It is remarkable that the polarization-dependent SHG intensity of the  $\text{WS}_2/\text{Si}/\text{Au}$  nanocavity exhibits a nonuniform 4-fold petals and unsymmetrical polar pattern, which is much different from that of the  $\text{WS}_2$  monolayer. This indicates that the second order nonlinear optical responses of the  $\text{WS}_2$  monolayer is significantly modified by the anisotropic strain. Theoretical studies indicate that a TMDC monolayer usually exhibits an anisotropic mechanical response to the strains along the zig-zag (ZZ) and armchair (AC) directions.<sup>[58]</sup> For example, the variation in the lattice structure of a  $\text{MoS}_2$  monolayer under the strain along the ZZ direction is larger than that along the AC direction.<sup>[59]</sup> Thus, it is suggested that the combination of the anisotropic mechanical response of  $\text{WS}_2$  monolayer with the anisotropic strain induced

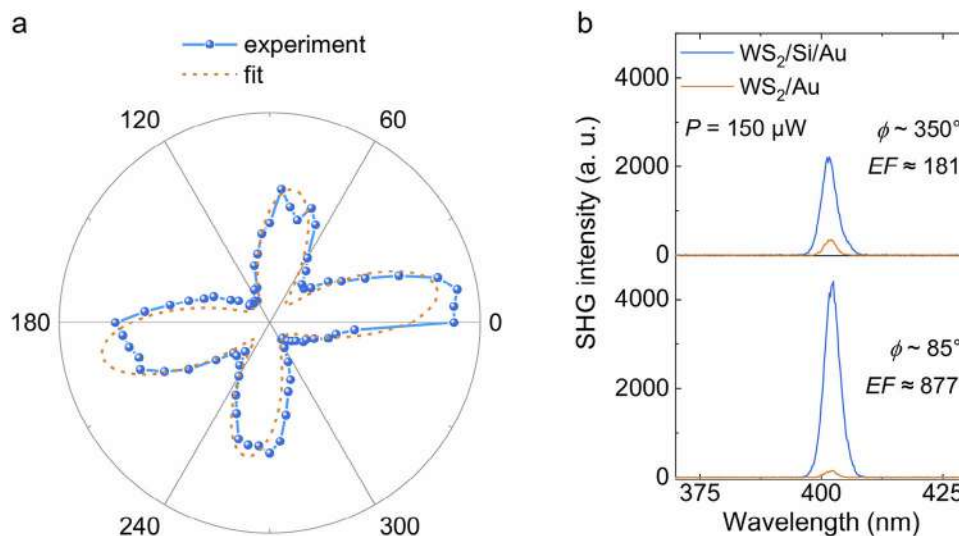


**Figure 5.** Polarization-dependent SHG intensity of a  $\text{WS}_2/\text{Si}/\text{Au}$  nanocavity. a) The dependence of the SHG intensity on excitation polarization angle measured for the  $\text{WS}_2/\text{Si}/\text{Au}$  nanocavity (nanocavity G) at  $\lambda_{\text{ex}} = 1064$  nm. Blue symbols represent the measured data, while the orange dashed line is the fitting curve. b) SHG spectra measured for the  $\text{WS}_2/\text{Si}/\text{Au}$  nanocavity (nanocavity G) and  $\text{WS}_2/\text{Au}$  planar structure at two excitation polarization angles ( $\phi$ ) and at  $\lambda_{\text{ex}} = 800$  nm. The  $EF$ s of the SHG intensity of the  $\text{WS}_2/\text{Si}/\text{Au}$  nanocavity are also provided.

by a specific Si/Au nanocavity leads to the complex polarization-dependent SHG intensity in the three  $\text{WS}_2/\text{Si}/\text{Au}$  nanocavities (see Figure 5a; Note S13, Supporting Information). In Figure 5a, we also show the fitting of the experimental data based on the photoelastic equation (orange dashed curve) (see Note S13, Supporting Information), which is applicable to the  $\text{WS}_2$  monolayer imposed by uniform strain. This behavior indicates that the  $EF$  of SHG intensity of a strained  $\text{WS}_2/\text{Si}/\text{Au}$  nanocavity can be manipulated by simply changing the polarization angle of the excitation light. We performed SHG measurements for the  $\text{WS}_2/\text{Si}/\text{Au}$  nanocavity at  $\lambda_{\text{ex}} = 800$  nm and only at two polarization angles in this case, as shown in Figure 5b. It is found that the  $EF$  of SHG of the  $\text{WS}_2/\text{Si}/\text{Au}$  nanocavity is reduced dramatically from  $\approx 877$  to  $\approx 181$  when the polarization angle is changed from  $85^\circ$  to  $350^\circ$ . It confirms that the anisotropic second-order nonlinear optical responses of the  $\text{WS}_2/\text{Si}/\text{Au}$  nanocavity is induced by the non-uniform strain.

### 3. Conclusion

In summary, we systematically studied the impact of non-uniform and spatially localized strain on the nonlinear optical responses of a  $\text{WS}_2$  monolayer induced by a Si/Au nanocavity. We find that the PL and SHG intensities of a strained  $\text{WS}_2/\text{Si}/\text{Au}$  nanocavity can be greatly enhanced, and the  $EF$ s are closely related to the magnitude of strain. We confirmed that the enhanced PL intensity originates from the exciton funneling effect, and the significant enhancement in SHG intensity arises from the strain-modified nonlinear susceptibility of the  $\text{WS}_2$  monolayer induced by the non-uniform strain. We revealed the strong dependence of the SHG intensity of a  $\text{WS}_2/\text{Si}/\text{Au}$  nanocavity on the excitation wavelength and the polarization angle of the excitation light. We observed that the  $EF$  of SHG of a  $\text{WS}_2/\text{Si}/\text{Au}$  nanocavity is as large as  $\approx 9649$ . The enhanced SHG observed in a strained  $\text{WS}_2$

monolayer induced by a Si/Au nanocavity will benefit for the realization of quantum circuits based on 2D materials. In addition, the study of strain-induced modification in SHG in TMDC monolayers can be further extended to third harmonic generation and four-wave mixing, which are also important in nonlinear optical devices. Moreover, nanoparticles with specific shapes, such as nanocylinders and nanocones, can be employed to apply quantitative strain on TMDC monolayers. In order to achieve isotropic and reproducible nanocavity-induced strain in TMDC monolayers, one can consider to replace silicon nanoparticles used in this work with polystyrene nanospheres with controllable sizes and smooth surfaces in the future research and application.

### 4. Experimental Section

**Sample Preparation:** The silicon nanoparticles with different diameters were fabricated by using fs laser ablation.<sup>[60]</sup> The 800 nm fs laser pulse (Legend, Coherent) with a duration of 100 fs and a repetition rate of 1 kHz was employed to ablate the silicon wafer which immersed in deionized water. The aqueous solution of silicon nanoparticles was dropped on the Au/SiO<sub>2</sub> substrate (with a 50 nm thick gold film) and dried naturally, obtaining the Si/Au nanocavities operating at different wavelengths. A wet-transfer approach was then employed to transfer the  $\text{WS}_2$  monolayers grown by CVD onto the Si/Au nanocavities, creating the  $\text{WS}_2/\text{Si}/\text{Au}$  nanocavities. First, a thin film of poly(methyl methacrylate) (PMMA) was spin-coated onto the  $\text{WS}_2$  monolayers grown on a SiO<sub>2</sub>/Si substrate. Then, the PMMA/ $\text{WS}_2$  film was separated from the SiO<sub>2</sub>/Si substrate by etching with KOH (2 mol L<sup>-1</sup>) at 80 °C. After removing the residual KOH by deionized water, the PMMA/ $\text{WS}_2$  film was transferred onto the Si/Au nanocavities and soaked in acetone to dissolve the PMMA layer, obtaining the  $\text{WS}_2$  monolayers on the Si/Au nanocavities. As compared with metallic substrates, it was relatively difficult to introduce strain in a  $\text{WS}_2$  monolayer by using dielectric substrates, such as ITO/SiO<sub>2</sub> and Al<sub>2</sub>O<sub>3</sub> substrates. The reason might be the large roughness of the dielectric substrates or the smaller van der Waals force between the  $\text{WS}_2$  monolayer and the dielectric substrate (see Note S8, Supporting Information). In our case, the

emission of defect-bound excitons were not observed in the PL spectra of the  $WS_2$  monolayers used in this study, indicating that the defects or impurities in the  $WS_2$  monolayers grown by CVD were quite small.

**Optical Characterization:** The linear and nonlinear optical responses of the  $WS_2/Si/Au$  nanocavities were measured by using an inverted microscope (Observer A1, Zeiss) equipped with a color CCD (DS-Ri2, Nikon) and a spectrometer (SR500i-B1, Andor). For the PL measurements, a 488 nm CW laser beam was introduced into the microscope and focused on the  $WS_2/Si/Au$  nanocavities or the  $WS_2/Au$  planar structures by using a 50 $\times$  objective. For the SHG measurements, the  $WS_2/Si/Au$  nanocavities or  $WS_2/Au$  planar structures were excited by the fs laser light focused with the 100 $\times$  objective of the microscope. The SHG mapping of the  $WS_2/Si/Au$  nanocavities and  $WS_2/Au$  planar structures was performed by using a confocal laser scanning microscope (ATMP, Nikon). The Raman spectra of the  $WS_2/Si/Au$  nanocavities and  $WS_2/Au$  planar structures were measured by using a Raman spectrometer (LabRAM HR Evolution, Horiba) equipped with a 300 g mm<sup>-1</sup> grating and the 100 $\times$  objective of the microscope.

**Numerical Simulations:** In this work, the numerical simulations were performed by using the finite-difference time-domain technique (FDTD). The boundary condition used in the FDTD simulations was the perfectly matched layer. Due to the symmetry of the structure and light source, anti-symmetry and symmetry were respectively set in the x and y directions. The dielectric constants of gold, silicon, and  $WS_2$  monolayer were taken from literatures.<sup>[61,62]</sup> The refractive index of the surrounding media was chosen to be 1.0. In the calculation, the thickness of the  $WS_2$  monolayer was chosen to be 1.0 nm. The mesh sizes in the  $WS_2$  monolayer, the gap between the silicon nanoparticle and the gold film, and the other region were set to be 0.2, 1, and 5 nm, respectively.

## Supporting Information

Supporting Information is available from the Wiley Online Library or from the author.

## Acknowledgements

This work was financially supported by the National Natural Science Foundation of China (Grant Nos. 12174123 and 12374347) and the Guangdong Basic and Applied Basic Research Foundation (Grant No. 2025A1515012291).

## Conflict of Interest

The authors declare no conflict of interest.

## Data Availability Statement

The data that support the findings of this study are available from the corresponding author upon reasonable request.

## Keywords

nanocavity, second harmonic generation, strain, symmetry breaking, transition metal dichalcogenide

Received: March 2, 2025

Revised: April 22, 2025

Published online:

[1] T. Helk, E. Berger, S. Jamnuch, L. Hoffmann, A. Kabacinski, J. Gautier, F. Tissandier, J. P. Goddet, H. T. Chang, J. Oh, C. Das Pemmaraju, T. A. Pascal, S. Sebban, C. Spielmann, M. Zuerch, *Sci. Adv.* **2021**, *7*, 2265.

- [2] S. Shwartz, M. Fuchs, J. B. Hastings, Y. Inubushi, T. Ishikawa, T. Katayama, D. A. Reis, T. Sato, K. Tono, M. Yabashi, S. Yudovich, S. E. Harris, *Phys. Rev. Lett.* **2014**, *112*, 163901.
- [3] T. Manaka, E. Lim, R. Tamura, M. Iwamoto, *Nat. Photonics* **2007**, *1*, 581.
- [4] X. Yin, Z. Ye, D. A. Chenet, Y. Ye, K. O'Brien, J. C. Hone, X. Zhang, *Science* **2014**, *344*, 488.
- [5] Y. Shen, *Nature* **1989**, *337*, 519.
- [6] D. Hsieh, J. W. McIver, D. H. Torchinsky, D. R. Gardner, Y. S. Lee, N. Gedik, *Phys. Rev. Lett.* **2011**, *106*, 057401.
- [7] J. Y. Chauleau, E. Haltz, C. Carrétero, S. Fusil, M. Viret, *Nat. Mater.* **2017**, *16*, 803.
- [8] K.-Q. Lin, S. Bange, J. M. Lupton, *Nat. Phys.* **2019**, *15*, 242.
- [9] H. Hong, C. Huang, C. Ma, J. Qi, X. Shi, C. Liu, S. Wu, Z. Sun, E. Wang, K. Liu, *Phys. Rev. Lett.* **2023**, *131*, 233801.
- [10] W. Huang, Y. Xiao, F. Xia, X. Chen, T. Zhai, *Adv. Funct. Mater.* **2024**, *34*, 2310726.
- [11] W. T. Hsu, Z. A. Zhao, L. J. Li, C. H. Chen, M. H. Chiu, P. S. Chang, Y. C. Chou, W. H. Chang, *ACS Nano* **2014**, *8*.
- [12] I. Abdelwahab, B. Tilmann, Y. Wu, D. Giovanni, I. Verzhbitskiy, M. Zhu, R. Berté, F. Xuan, L. d. S. Menezes, G. Eda, T. C. Sum, S. Y. Quek, S. A. Maier, K. P. Loh, *Nat. Photonics* **2022**, *16*, 644.
- [13] H. G. Rosa, L. Junpeng, L. C. Gomes, M. J. L. F. Rodrigues, S. C. Haur, J. C. V. Gomes, *Adv. Opt. Mater.* **2018**, *6*, 1701327.
- [14] H. Jiang, L. Zheng, J. Wang, M. Xu, X. Gan, X. Wang, W. Huang, *Nanoscale* **2021**, *13*, 18103.
- [15] H. Yu, D. Talukdar, W. Xu, J. B. Khurgin, Q. Xiong, *Nano Lett.* **2015**, *15*, 5653.
- [16] Z. Sun, Y. Yi, T. Song, G. Clark, B. Huang, Y. Shan, S. Wu, D. Huang, C. Gao, Z. Chen, M. McGuire, T. Cao, D. Xiao, W.-T. Liu, W. Yao, X. Xu, S. Wu, *Nature* **2019**, *572*, 497.
- [17] J. Feng, X. F. Qian, C. W. Huang, J. Li, *Nat. Photonics* **2012**, *6*, 865.
- [18] K. He, C. Poole, K. F. Mak, J. Shan, *Nano Lett.* **2013**, *13*, 2931.
- [19] H. J. Conley, B. Wang, J. I. Ziegler, R. F. Haglund, S. T. Pantelides, K. I. Bolotin, *Nano Lett.* **2013**, *13*, 3626.
- [20] Y. Wang, C. Cong, W. Yang, J. Shang, N. Peimyoo, Y. Chen, J. Kang, J. Wang, W. Huang, T. Yu, *Nano Res.* **2015**, *8*, 2562.
- [21] R. Ghosh, B. Papnai, Y. S. Chen, K. Yadav, R. Sankar, Y. P. Hsieh, M. Hofmann, Y. F. Chen, *Adv. Mater.* **2023**, *35*, 2210746.
- [22] Z. W. Peng, X. L. Chen, Y. L. Fan, D. J. Srolovitz, D. Y. Lei, *Light Sci. Appl.* **2020**, *9*, 190.
- [23] D. Akinwande, N. Petrone, J. Hone, *Nat. Commun.* **2014**, *5*, 5678.
- [24] Z. Li, Y. Lv, L. Ren, J. Li, L. Kong, Y. Zeng, Q. Tao, R. Wu, H. Ma, B. Zhao, D. Wang, W. Dang, K. Chen, L. Liao, X. Duan, X. Duan, Y. Liu, *Nat. Commun.* **2020**, *11*, 1151.
- [25] S. Roy, X. D. Yang, J. Gao, *Sci. Rep.* **2024**, *14*, 3860.
- [26] A. Castellanos-Gomez, R. Roldan, E. Cappelluti, M. Buscema, F. Guinea, H. S. van der Zant, G. A. Steele, *Nano Lett.* **2013**, *13*.
- [27] K. P. Dhakal, S. Roy, H. Jang, X. Chen, W. S. Yun, H. Kim, J. Lee, J. Kim, J.-H. Ahn, *Chem. Mater.* **2017**, *29*, 5124.
- [28] A. V. Tyurnina, D. A. Bandurin, E. Khestanova, V. G. Kravets, M. Koperski, F. Guinea, A. N. Grigorenko, A. K. Geim, I. V. Grigorieva, *ACS Photonics* **2019**, *6*, 516.
- [29] T. P. Darlington, C. Carmesin, M. Florian, E. Yanev, O. Ajayi, J. Ardelean, D. A. Rhodes, A. Ghiotto, A. Krayev, K. Watanabe, T. Taniguchi, J. W. Kysar, A. N. Pasupathy, J. C. Hone, F. Jahnke, N. J. Borys, P. J. Schuck, *Nat. Nanotechnol.* **2020**, *15*, 854.
- [30] S. Shabani, T. P. Darlington, C. Gordon, W. Wu, E. Yanev, J. Hone, X. Zhu, C. E. Dreyer, P. J. Schuck, A. N. Pasupathy, *Nano Lett.* **2022**, *22*, 7401.
- [31] H. Li, A. W. Contryman, X. Qian, S. M. Ardakani, Y. Gong, X. Wang, J. M. Weisse, C. H. Lee, J. Zhao, P. M. Ajayan, J. Li, H. C. Manoharan, X. Zheng, *Nat. Commun.* **2015**, *6*, 7381.

- [32] J. Chaste, A. Missaoui, S. Huang, H. Henck, Z. Ben Aziza, L. Ferlazzo, C. Naylor, A. Balan, A. T. C. Johnson, R. Braive, A. Ouerghi, *ACS Nano* **2018**, *12*, 3235.
- [33] A. Kayal, S. Dey, H. G., R. Nadarajan, S. Chattopadhyay, J. Mitra, *Nano Lett.* **2023**, *23*, 6629.
- [34] T. Chowdhury, K. Jo, S. B. Anantharaman, T. H. Brintlinger, D. Jariwala, T. J. Kempa, *ACS Photonics* **2021**, *8*, 2220.
- [35] S. Li, K. K. Chui, F. Shen, H. Huang, S. Wen, C. Yam, L. Shao, J. Xu, J. Wang, *ACS Nano* **2022**, *16*, 10647.
- [36] M. G. Harats, J. N. Kirchhof, M. Qiao, K. Greben, K. I. Bolotin, *Nat. Photonics* **2020**, *14*, 324.
- [37] J. Lee, S. J. Yun, C. Seo, K. Cho, T. S. Kim, G. H. An, K. Kang, H. S. Lee, J. Kim, *Nano Lett.* **2020**, *21*, 43.
- [38] D. Zhang, L. Gan, J. Zhang, R. Zhang, Z. Wang, J. Feng, H. Sun, C. Z. Ning, *ACS Nano* **2020**, *14*, 6931.
- [39] C. He, R. Wu, L. Zhu, Y. Huang, W. Du, M. Qi, Y. Zhou, Q. Zhao, X. Xu, *J. Phys. Chem. Lett.* **2022**, *13*, 352.
- [40] J. Liang, J. Zhang, Z. Li, H. Hong, J. Wang, Z. Zhang, X. Zhou, R. Qiao, J. Xu, P. Gao, Z. Liu, Z. Sun, S. Meng, K. Liu, D. Yu, *Nano Lett.* **2017**, *17*, 7539.
- [41] L. Mennel, M. M. Furchi, S. Wachter, M. Paur, D. K. Polyushkin, T. Mueller, *Nat. Commun.* **2018**, *9*, 516.
- [42] L. Mennel, M. Paur, T. Mueller, *APL Photonics* **2019**, *4*, 034404.
- [43] J. Wang, M. Han, Q. Wang, Y. Ji, X. Zhang, R. Shi, Z. Wu, L. Zhang, A. Amini, L. Guo, N. Wang, J. Lin, C. Cheng, *ACS Nano* **2021**, *15*, 6633.
- [44] S. Rachel, I. Göthel, D. P. Arovass, M. Vojta, *Phys. Rev. Lett.* **2016**, *117*, 266801.
- [45] K. Lu, M. Luo, W. Gao, Q. J. Wang, H. Sun, D. Nam, *Nat. Commun.* **2023**, *14*, 2580.
- [46] S. Rahman, T. Yildirim, M. Tebyetekerwa, A. R. Khan, Y. Lu, *ACS Nano* **2022**, *16*, 13959.
- [47] T. Fu, K. Bu, X. Sun, D. Wang, X. Feng, S. Guo, Z. Sun, Y. Fang, Q. Hu, Y. Ding, T. Zhai, F. Huang, X. Lü, *J. Am. Chem. Soc.* **2023**, *145*, 16828.
- [48] X. Han, K. Wang, P. D. Persaud, X. Xing, W. Liu, H. Long, F. Li, B. Wang, M. R. Singh, P. Lu, *ACS Photonics* **2020**, *7*, 562.
- [49] F. Spreyer, C. Ruppert, P. Georgi, T. Zentgraf, *ACS Nano* **2021**, *15*, 16719.
- [50] F. J. F. Löchner, A. George, K. Koshelev, T. Bucher, E. Najafdehaghani, A. Fedotova, D.-Y. Choi, T. Pertsch, I. Staude, Y. Kivshar, A. Turchanin, F. Setzpfandt, *ACS Photonics* **2020**, *8*, 218.
- [51] J. Shi, X. Wu, K. Wu, S. Zhang, X. Sui, W. Du, S. Yue, Y. Liang, C. Jiang, Z. Wang, W. Wang, L. Liu, B. Wu, Q. Zhang, Y. Huang, C.-W. Qiu, X. Liu, *ACS Nano* **2022**, *16*, 13933.
- [52] H. Li, Y. Xu, J. Xiang, X. F. Li, C. Y. Zhang, S. L. Tie, S. Lan, *Nanoscale* **2016**, *8*, 18963.
- [53] S. Liu, F. Deng, W. Zhuang, X. He, H. Huang, J. D. Chen, H. Pang, S. Lan, *ACS Nano* **2022**, *16*, 14390.
- [54] Y. Yu, Y. Yu, C. Xu, Y. Q. Cai, L. Su, Y. Zhang, Y. W. Zhang, K. Gundogdu, L. Cao, *Adv. Funct. Mater.* **2016**, *26*, 4733.
- [55] Y. Sun, R. Wang, K. Liu, *Appl. Phys. Rev.* **2017**, *4*, 011301.
- [56] H. Lee, Y. Koo, S. Kumar, Y. Jeong, D. G. Heo, S. H. Choi, H. Joo, M. Kang, R. H. Siddique, K. K. Kim, H. S. Lee, S. An, H. Choo, K.-D. Park, *Nat. Commun.* **2023**, *14*, 1891.
- [57] K. Beach, M. C. Lucking, H. Terrones, *Phys. Rev. B* **2020**, *101*, 155431.
- [58] Q. Peng, S. De, *Phys. Chem. Chem. Phys.* **2013**, *15*, 19427.
- [59] R. C. Cooper, C. Lee, C. A. Marianetti, X. D. Wei, J. Hone, J. W. Kysar, *Phys. Rev. B.* **2013**, *87*, 035423.
- [60] C.-Q. Li, C.-Y. Zhang, Z.-S. Huang, X.-F. Li, Q.-F. Dai, S. Lan, S.-L. Tie, *J. Phys. Chem. C.* **2013**, *117*, 24625.
- [61] P. B. Johnson, R. W. Christy, *Phys. Rev. B.* **1972**, *6*, 4370.
- [62] Y. Li, A. Chernikov, X. Zhang, A. Rigosi, H. M. Hill, A. M. van der Zande, D. A. Chenet, E.-M. Shih, J. Hone, T. F. Heinz, *Phys. Rev. B.* **2014**, *90*, 205422.